Effects of Planet Curvature and Crust on the Shock Pressure Field Around Impact Basins

Effects of Planet Curvature and Crust on the Shock Pressure Field around Impact Basins

Karin L. Louzada, Sarah T. Stewart

Department of Earth and Planetary Sciences, Harvard University, Cambridge, MA, USA.

Geophysical Research Letters, accepted, July 2009.

Abstract

We investigate the effects of planetary curvature and the crust-mantle boundary on the shock pressure field around impact basins on Mars using acoustic ray path calculations and hydrocode simulations. Planet curvature and, to a lesser extent, increasing sound speed with depth shallow the zone of wave interference, where shock pressures decay rapidly to the surface. The depth to the interference zone boundary diverges from the flat surface solution for projectile-to-Mars radius ratios greater than ~1% (transient craters greater than ~300 km); the difference increases with distance from the impact point and projectile size. In hydrocode simulations (but not the simple ray path model), the presence of the crust-mantle boundary produces nearly vertical pressure contours in the crust. Around Hellas basin, demagnetization occurs at shock pressures between 1.1 (±0.2) and 3.4 (±0.7) GPa, where the range is due to the uncertainty in the transient crater diameter.

1. Introduction

Recent interest in the shock pressure field around impact basins has been fueled by observations of unmagnetized crust around the younger basins on Mars [e.g., Hellas basin, *Acuña, et al.*, 1999] coupled with experimental evidence of pressure demagnetization of magnetic minerals at a few GPa [e.g., *Hargraves and Perkins*, 1969; *Nagata*, 1974; *Cisowski and Fuller*, 1978; *Rochette, et al.*, 2003; *Kletetschka, et al.*, 2004; *Gattacceca, et al.*, 2007; *Louzada, et al.*, 2007]. It is hoped that understanding shock demagnetization will provide constraints on the mineralogy of the crust [*Cisowski and Fuller*, 1978; *Kletetschka, et al.*, 2004; *Bezaeva, et al.*, 2007].

Near the surface around impact craters, compressive waves and rarefaction waves reflected from the planet's surface interact, leading to a zone of reduced shock pressure [*Melosh*, 1984]. The shock pressure distribution in the crust is sensitive to the geometry of this interference zone. Previous estimates of the shock pressure distribution in the crust surrounding Martian impact basins have not included an interference zone [*Hood, et al.*, 2003] or used an adaptation of the stress wave propagation and reflection model for flat homogeneous surfaces by Melosh [1984] [e.g., *Kletetschka, et al.*, 2004; *Mohit and Arkani-Hamed*, 2004].

In this work, we investigate the effects of planet curvature and the crust-mantle boundary on the geometry of the interference zone and the shock pressure distribution in the crust around large impact events. We perform numerical wave propagation calculations and solve for shock pressures in the interference zone. We compare ray path results for a Hellas-size event to two- and three-dimensional simulations using the hydrocode CTH [*McGlaun, et al.*, 1990]. Finally, we discuss the implications for shock demagnetization on Mars.

2. Method: Near-Surface Pressure Field

2.1 Interference Zone Boundary (IZB) for a Flat Surface

The stress wave propagation and reflection model of Melosh [1984] likens the impact to an explosion centered at burial depth, d. At any point in the subsurface, shock waves emitted from this point are followed by reflected waves from the planet's surface with an arrival time delay, Δt. The pressure history of the material can be approximated as the sum of the two waves (Figure 1). In the interference zone, the arrival time difference between the two waves is less than the shock rise time ($\Delta t < \tau$), and the peak shock pressure is reduced. The interference zone boundary is defined where $\Delta t = \tau$.

Melosh [1984] calculated the depth of the interference zone boundary (D_{IZB}) as a function of distance along the surface, s:

$$D_{\mathrm{IZB}}(s) = c_{\mathrm{L}}\tau\left[\left(4\left(d^2+s^2\right)-{c_{\mathrm{L}}}^2\tau^2\right)\Big/\left(4d^2-{c_{\mathrm{L}}}^2\tau^2\right)\right]^{1/2} \quad (1)$$

τ is approximated by $r_{\mathrm{pr}}/v_{\mathrm{i}}$; r_{pr} is the projectile radius, v_{i} is the impact velocity and $d = 0.7 \cdot r_{\mathrm{pr}}$ [*Pierazzo, et al.*, 1997]. The waves are assumed to travel at a constant longitudinal sound speed, c_{L}.

Previous pressure field estimates around impact basins on Mars using Equation 1 differed in (i) the value of d, (ii) the impact conditions (projectile diameter and velocity), and (iii) the method for calculating the reduced pressure in the interference zone, either a linear decay to the surface from the maximum pressure at depth [*Kletetschka, et al.*, 2004] or summing of two triangular-shaped waves (a function of Δt and τ [*Mohit and Arkani-Hamed*, 2004]). These studies did not include two potentially important factors. First, due to curvature of the planet's surface, the difference in path length (and arrival time) between the direct and reflected waves is larger in a spherical planet than in a flat planet (Figure S1, auxiliary material). Second, the interference

zone may be affected by variable wave speeds and the presence of the crust-mantle boundary.

2.2 Ray Path Model for a Spherical Planet

Here, we incorporate flat and spherical planet geometries in ray path calculations to solve for the interference zone boundary. Mars is modeled with three internal structures (Figure S2): (I) homogeneous (crust only), (II) heterogeneous with a 50-km thick crust, 2000-km thick mantle, and 1376–km radius core, and (III) heterogeneous without a crust (the mantle extends to the surface). Waves are propagated radially away from the burial point and refracted or reflected according to the local longitudinal sound speed. The propagation time step is constrained by the cell size in a two-dimensional grid (rectangular or polar). In each grid cell, the arrival times and ray path lengths of the compressive and reflected waves are collected, and the depth to the interference zone boundary is determined. Grid resolution, angle spacing and time step sensitivity tests are shown in Figure S3.

2.3 Shock Pressure Decay

In the ray path calculation, the amplitude of the waves is assumed to decay as a function of the total distance traveled, l. The maximum shock pressure occurs near the impact point in the isobaric core (P_{ibc}, ~130 GPa for basaltic materials and typical impact velocities of 9 km/s for Mars [*Ivanov*, 2001]). Outside of the isobaric core, the shock pressure amplitude decays exponentially as a (segmented) power-law with distance [*Ahrens and O'Keefe*, 1987; *Pierazzo, et al.*, 1997]. Figure 2 shows the results of shock pressure decay with distance from CTH simulations using the impact conditions described in section 3.1. Since we are interested in the few GPa pressure regime and Pierazzo et al.'s [1997] scaling laws do not extend past $5 \cdot r_{\mathrm{pr}}$, we utilize the pressure decay results from the CTH simulations in the ray path calculations.

In each grid cell, the pressures of the direct ($P > 0$) and reflected ($P < 0$) rays are determined

from their path lengths and the pressure function. The effective pressure, P_{eff}, in cells located in the interference zone is a function of the arrival time difference of the waves [after *Melosh*, 1984]:

$$P_{\text{eff}} = P(l_{\text{D}}) + P(l_{\text{R}})(1 - \Delta t/\tau), \quad (2)$$

where l_{D} and l_{R} are the total distances that the direct and reflected waves have traveled (scaled by projectile size), respectively.

3. Results

3.1 A Hellas Forming Impact

Hellas is an example of a basin clearly devoid of crustal magnetization [*Acuña, et al.*, 1999]. In order to derive the shock pressure field around Hellas, we need to estimate the impact conditions and therefore its transient crater. Hellas basin is elliptical with inner (floor) and outer (rim-to-rim) topographic boundaries of 1400-2000 km and 1900-2300 km, respectively. Previous workers [*Hood, et al.*, 2003; *Kletetschka, et al.*, 2004; *Mohit and Arkani-Hamed*, 2004] have assumed that the transient basin diameter is comparable to the inner topographic boundary (~1300-1500 km), which must be an upper limit. We initially make the same assumption here.

Using Π-scaling for flat surfaces [e.g. *Melosh*, 1989, Section 7.7; *Melosh and Beyer*, 1998], a 230-km radius asteroid (3000 kg/m^3) at a typical (vertical) impact velocity of 9 km/s onto Mars (3000 kg/m^3) produces a 1250-km diameter transient crater in competent rock. Hydrodynamic CTH calculations (auxiliary material) using the same impact parameters produce transient crater diameters of 1300-1400 km.

3.2 IZB for a Flat versus Spherical Homogeneous Planet

First we consider a homogenous planet (case I) to assess the effect of planet curvature. Using

the ray path model, we compare the depth to the interference zone boundary, $D_{IZB,}$ for a flat and spherical Mars. The blue (online) or grey (in print) dots in Figure 3A show D_{IZB} for an impact on a homogeneous Mars by a 230-km radius projectile at 9 km/s (a Hellas-type event). (Note that D_{IZB} is independent of the pressure decay profile.) The results indicate that the IZB is shallower in a spherical planet and that the depth to the boundary decreases with increasing distance and impactor size (Figure 3B). For example, the IZB is reduced by approximately 40% for the Hellas-type event: a 230-km radius projectile and a distance of ~1000 km (4 r_{pr}, right-most diamonds in Figure 3B), the radius of the demagnetized zone (see section 4.2).

3.3 IZB for a Flat versus Spherical Heterogeneous Planet

Calculations using a full Mars interior model (heterogeneous case II, red (online) or black (in print) dots in Figure 3A) produce IZBs that are slightly shallower than those for a homogeneous Mars, for both spherical and flat planet geometries. The depth to the IZB is more sensitive to the planet curvature than the increasing longitudinal sound speed with depth. In fact, the change in depth of the IZB due to planet geometry is nearly independent of the internal structure of the planet for all projectile radii and distances (compare the red and blue (online) or grey and black (in print) symbols in Figure 3B).

3.4 Pressure Field around Hellas Basin and the Effect of the Crust-Mantle Boundary

In Figure 4, we present shock pressure contours using both the ray path model (solid lines) and the CTH calculations (dashed lines), and the Hellas impact conditions described above, for the upper 100 km of a (A) flat and (A) spherical Mars. Magnetization in the lower crust of Mars has likely been reduced due to viscous relaxation in the absence of an ambient field [*Shahnas and Arkani-Hamed*, 2007]. Also, the upper crust has been demagnetized by a combination of primary impacts [*Shahnas and Arkani-Hamed*, 2007] and secondaries from impact basins greater

than ~500 km diameter [*Artemieva, et al.*, 2005]. It is assumed that the magnetic crust is located between 10 and 50 km depth [*Dunlop and Arkani-Hamed*, 2005] (Figure 4). In both the ray path and CTH results, the pressure contours in the spherical planet are indeed closer to the surface than in the flat planet. However, for both the flat and spherical planet, the CTH pressure contours are steeper in the crust and deeper in the mantle compared to the ray path model. In contrast, ray path and CTH simulations for flat heterogeneous planets without a crust (case III) are of similar shape (Figure S4); thus the ray path model does not adequately capture crust-mantle boundary effects.

The differences between pressure contours from ray path calculations and CTH simulations are likely due to the fact that the burial depth and shock wave rise times are not truly constant. For example, the burial depth increases with decreasing shock pressure (Figure S5). Additionally, the assumption of interference of only two waves and/or the wave shape may be too simple.

4. Discussion

4.1 Implications for Impact Basin Formation

The depth to the interference zone boundary begins to diverge from the flat surface solution (by more than ~10%) for projectile radii of 25 to 50 km, corresponding to a projectile-to-planet radius ratio of ~1% (Figure 3B). Using Π-scaling developed for (smaller) complex craters, vertical impacts at 9 km/s of such impactors will produce transient craters with diameters of 221 to 380 km on Mars and final crater diameters of 700 to 1300 km [*Melosh and Beyer*, 1998]. On Mars, approximately 20 craters are of this size or larger [*Frey*, 2008].

The relationship between such large impact basins and the impact conditions that formed them

is highly uncertain [*Melosh*, 1989, Chapter 7]. Impact basins are morphologically very different from simple and complex craters, and extensive modification during collapse makes estimation of the transient crater diameter difficult. In addition, here we only consider vertical impacts; average (45°) oblique impacts will displace the region of intense shock to shallower depths and in the downrange direction, but have little effect on the far-field lower shock pressures [*Pierazzo and Melosh*, 2000].

The assumption that complex crater scaling continues into the basin regime is as valid as (and perhaps better than) the assumption of using the inner scarp to estimate the transient basin. The transient basin of Hellas was likely much smaller than its present-day flat floor. Using the geometric reconstruction for complex craters [*Melosh*, 1989, Eq. 8.3.1] and a basin depth of ~10 km, we estimate a lower limit for the transient basin size of Hellas at about 800 km. This value is considerably smaller than the previously assumed upper limit of 1300-1500 km. In this end-member case, using the same impact conditions, the impactor radius is only 125 km.

4.2 Implications for the Martian Magnetic Crust

Hood et al. [2003] estimate that extensive demagnetization (~90%) occurred out to 3-4 basin radii (~2 GPa) and that significant demagnetization (~50%) occurred at 1 GPa or less (r_{pr} = 343-232 km, v_i = 7.5-15 km/s). By taking into account an interference zone, Kleteschka et al. [2004] estimate 60-70% impact demagnetization occurred at 1-2 basin radii (>1 GPa) (r_{pr} = 260 km, v_i = 15 km/s). Both studies assume impact angles of 45°, but symmetric pressure decay with distance. Mohit and Arkani-Hamed [2004] also considered an interference zone and estimated that partial demagnetization extends out to 1.2-1.4 basin radii (<0.5-1 GPa) and complete demagnetization occurred within ~0.8 basin radii (2-5 GPa) (r_{pr} = 210-230 km, v_i = 10-12 km/s). An upper limit on the radius of complete demagnetization was found by Lillis et al. [2009] to be 1.18 basin

radii, based on modeling of crustal magnetic intensity.

2-GPa pressure contour results from 3D-CTH simulations, using both the 230 and 125-km radius projectiles at 9 km/s, and from the previous studies are shown in Figure 4C. The results from this work bracket those of Mohit and Arkani-Hamed [2004] and Kletetschka, et al. [2004]. If demagnetization extends out to 1.4 basin radii, then at a radius of ~1000 km around Hellas the average shock pressure in the magnetic portion of the crust is between 1.1 (±0.2) and 3.4 (±0.7) GPa from CTH simulations, depending on the impactor size (Table S4). All candidate magnetic minerals (magnetite, hematite and pyrrhotite [*Dunlop and Arkani-Hamed*, 2005]) demagnetize in this pressure range [summarized in *Louzada*, 2009]. Considering the uncertainties in the transient basin diameter, at present, it is not possible to constrain impact demagnetization pressures and the magnetic mineralogy on Mars more precisely.

5. Conclusions

The onset of shallowing of the interference zone due to curvature begins at projectile-to-planet radius ratios of ~1%. Increasing sound speeds with depth results in additional shallowing of the interference zone with respect to homogeneous planets, but to a lesser extent. Shallowing of the interference zone leads to larger average shock pressures in the crust. These trends are observed in both ray path calculations and hydrocode simulations of impact basin formation. However, modification of the shape of shock pressure contours by the crust-mantle boundary is not captured in the ray path model. Based on the range of possible transient basin diameters and impact conditions, shock demagnetization around Martian impact basins occurred between 1.1 (±0.2) and 3.4 (±0.7) GPa.

Acknowledgements

Thanks to C. Dalton, D. Valencia, the Barringer Family Fund, the Amelia Earhart Fellowship (Zonta Int.), and two anonymous reviewers.

References

Acuña, M. H., J. E. P. Connerney, N. F. Ness, R. P. Lin, D. Mitchell, C. W. Carlson, J. McFadden, K. A. Anderson, H. Rème, C. Mazelle, D. Vignes, P. Wasilewski, and P. Cloutier (1999), Global Distribution of Crustal Magnetization Discovered by the Mars Global Surveyor MAG/ER Experiment, *Science*, *284*, 790-793, doi:10.1126/science.284.5415.790.

Ahrens, T. J., and J. D. O'Keefe (1987), Impact on the Earth, ocean and atmosphere, *Int. J. Impact Eng.*, *5*, 13-32, doi:10.1016/0734-743X(87)90028-5.

Artemieva, N., L. Hood, and B. A. Ivanov (2005), Impact demagnetization of the Martian crust: Primaries versus secondaries, *GRL*, *32*, doi:10.1029/2005GL024385.

Bezaeva, N. S., P. Rochette, J. Gattacceca, R. A. Sadykov, and V. I. Trukhin (2007), Pressure demagnetization of the Martian crust: Ground truth from SNC meteorites, *GRL*, *34*, L23202, doi:10.1029/2007GL031501.

Cisowski, S. M., and M. Fuller (1978), The Effect of Shock on the Magnetism of Terrestrial Rocks, *JGR*, *83*, 3441-3458.

Dunlop, D. J., and J. Arkani-Hamed (2005), Magnetic minerals in the Martian crust, *JGR*, *110*, E12S04, doi:10.1029/2005JE002404.

Frey, H. (2008), Ages of very large impact basins on Mars: Implications for the late heavy bombardment in the inner solar system, *GRL*, *35*, L13203, doi:10.1029/2008GL033515.

Gattacceca, J., A. Lamali, P. Rochette, M. Boustie, and L. Berthe (2007), The effects of explosive-driven shocks on the natural remanent magnetization and the magnetic properties of rocks, *PEPI*, *162*, 85-98, doi:10.1016/j.pepi.2007.1003.1006.

Hargraves, R. B., and W. E. Perkins (1969), Investigations of the Effect of Shock on Natural Remanent Magnetization, *JGR*, *74* (10), 2576-2589.

Hood, L. L., N. C. Richmond, E. Pierazzo, and P. Rochette (2003), Distribution of crustal magnetic fields on Mars: Shock effects of basin-forming impacts, *GRL*, *30*, 1281-1284, doi:10.1029/2002GL016657.

Ivanov, B. A. (2001), Mars/Moon cratering rate ratio estimates, *Space Sci. Rev.*, *96* (1-4), 87-104, doi:10.1023/A:1011941121102.

Kletetschka, G., J. E. P. Connerney, N. F. Ness, and M. H. Acuña (2004), Pressure effects on martian crustal magnetization near large impact basins, *MAPS*, *39*, 1839-1848.

Lillis, R. J., J. S. Halekas, K. L. Louzada, S. T. Stewart, and M. Manga (2009), Impact demagnetization at Mars: Using multiple altitude magnetic field data to constrain properties of crustal magnetization, *LPSC XL*, Abs. No. 1444.

Louzada, K. L. (2009), The effects of impact cratering on planetary crustal magnetism, Ph.D. thesis, 240 pp., Harvard University, Cambridge, June 4.

Louzada, K. L., S. T. Stewart, and B. P. Weiss (2007), Effect of shock on the magnetic properties of pyrrhotite, the Martian crust, and meteorites, *GRL*, *34*, L05204, doi:10.1029/2006GL027685.

McGlaun, J. M., S. L. Thompson, and M. G. Elrick (1990), CTH: A 3-dimensional shock-wave physics code, *Int. J. Impact Eng.*, *10*, 351-360, doi:10.1016/0734-743X(90)90071-3.

Melosh, H. J. (1984), Impact Ejection, Spallation, and the Origin of Meteorites, *Icarus*, *59*, 234-260, doi:10.1016/0019-1035(84)90026-5.

Melosh, H. J. (1989), *Impact Cratering: A Geologic Process*, 245 pp., Oxford University Press, New York.

Melosh, H. J., and R. A. Beyer (1998), Crater Program, edited.

Mohit, P. S., and J. Arkani-Hamed (2004), Impact demagnetization of the martian crust, *Icarus*,

168, 305-317, doi:10.1016/j.icarus.2003.12.005.

Nagata, T. (1974), Integrated Effect of Repeated Mechanical Shocks on Shock Remanent Magnetization and Shock Demagnetization, *Journal of Geophysics*, *40*, 467-487.

Pierazzo, E., and H. J. Melosh (2000), Melt Production in Oblique Impacts, *Icarus*, *145*, 252-261, doi:10.1006/icar.1999.6332.

Pierazzo, E., A. M. Vickery, and H. J. Melosh (1997), A Reevaluation of Impact Melt Production, *Icarus*, *127*, 408-423, doi:10.1006/icar.1997.5713.

Rochette, P., G. Fillion, R. Ballou, F. Brunet, B. Ouladdiaf, and L. Hood (2003), High pressure magnetic transition in pyrrhotite and impact demagnetization on Mars, *GRL*, *30*, doi:10.1029/2003GL017359.

Shahnas, H., and J. Arkani-Hamed (2007), Viscous and impact demagnetization of Martian crust, *JGR*, *112* (E02009), doi:10.1029/2005JE002424.

Figure 1. Schematic of interaction between triangular-shaped direct and reflected waves above, at, and below the interference zone boundary (IZB) [after *Melosh*, 1984]. The pressure history of the material is the sum of the two waves (thick solid line).

Figure 2. Shock pressure versus radial distance from a burial depth of $0.7 \cdot r_{pr}$ recorded by tracers below the interference zone in the crust and upper mantle (inset), for a 230-km radius projectile at 9 km/s. The 2D (triangles) and 3D (diamonds) results are nearly identical. Power-law exponents are indicated with standard deviations in parentheses.

Figure 3. (A) Depth to the interference zone boundary (D_{IZB}) for a 230-km radius projectile at 9 km/s into a flat and spherical, homogeneous (case I - blue) and heterogeneous (case II - red) Mars. The correlation between the homogeneous flat planet case and Equation 1 (dashed line) is $R^2 = 0.985$. (B) Ratio between $D_{IZB,\ Flat}$ and $D_{IZB,\ Sph}$ for different projectile-to-planet radius ratios (Table S3). We assume $\tau = r_{pr}/v_i$ (constant), $v_i = 9$ km/s, and $d = 0.7 \cdot r_{pr}$.

Figure 4. Shock pressure contours (5, 2 and 1 GPa) for a Hellas-size event using the ray path model (solid lines) and CTH hydrocode (dashed lines) for (A) flat and (B) spherical Mars geometries. 'IT' and 'OT' denote the inner and outer topographic boundary of Hellas, respectively. (C) 2-GPa shock pressure contours for a Hellas forming impact. See text for details. Vertical exaggeration = ~19x.

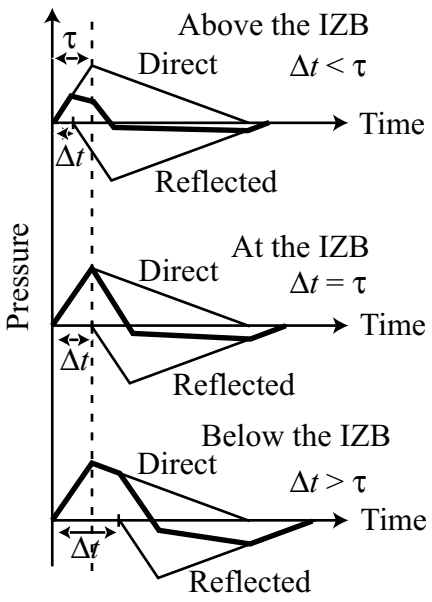
Above the IZB
τ
Direct
Δt < τ
Time
Δt
Reflected
At the IZB
Direct
Δt = τ
Time
Δt
Reflected
Below the IZB
Direct
Δt > τ
Time
Δt
Reflected
Pressure

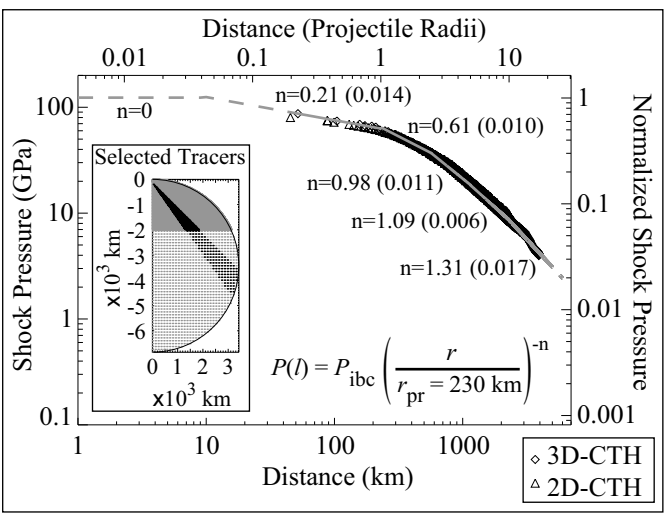
Distance (Projectile Radii)
0.01
0.1
1
10
Shock Pressure (GPa)
100
10
1
0.1
Normalized Shock Pressure
1
0.1
0.01
0.001
n=0
n=0.21 (0.014)
n=0.61 (0.010)
n=0.98 (0.011)
n=1.09 (0.006)
n=1.31 (0.017)
Selected Tracers
0
-1
-2
-3
-4
-5
-6
x10^3 km
0 1 2 3
x10^3 km
P(l) = P_ibc (r / r_pr = 230 km)^-n
1
10
100
1000
Distance (km)
3D-CTH
2D-CTH

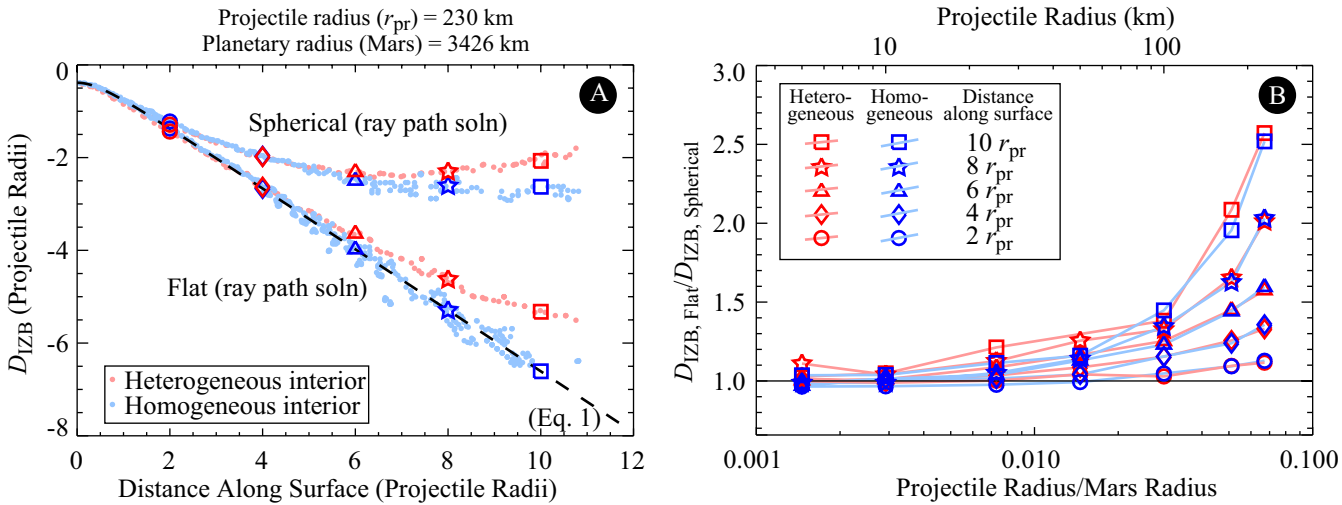
Projectile radius (r_{pr}) = 230 km
Planetary radius (Mars) = 3426 km
A
Spherical (ray path soln)
Flat (ray path soln)
Heterogeneous interior
Homogeneous interior
(Eq. 1)
D_{IZB} (Projectile Radii)
Distance Along Surface (Projectile Radii)
0
-2
-4
-6
-8
0
2
4
6
8
10
12
Projectile Radius (km)
10
100
B
Hetero-geneous
Homo-geneous
Distance along surface
10 r_{pr}
8 r_{pr}
6 r_{pr}
4 r_{pr}
2 r_{pr}
$D_{IZB, Flat}/D_{IZB, Spherical}$
3.0
2.5
2.0
1.5
1.0
0.001
0.010
0.100
Projectile Radius/Mars Radius

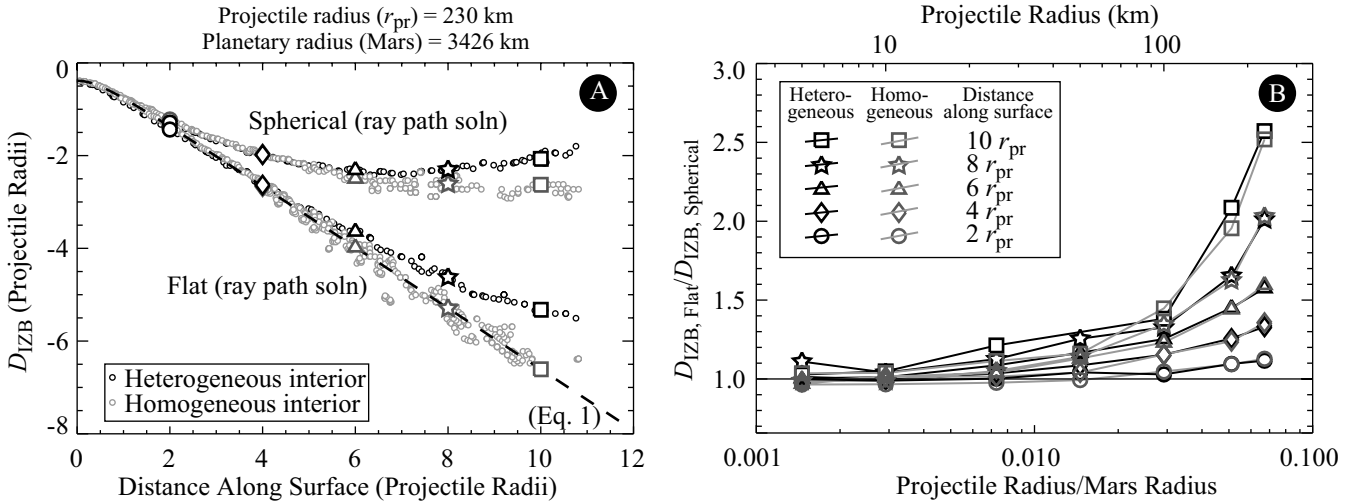
Projectile radius (r_{pr}) = 230 km
Planetary radius (Mars) = 3426 km
A
Spherical (ray path soln)
Flat (ray path soln)
Heterogeneous interior
Homogeneous interior
(Eq. 1)
D_{IZB} (Projectile Radii)
Distance Along Surface (Projectile Radii)
0
-2
-4
-6
-8
0
2
4
6
8
10
12
Projectile Radius (km)
10
100
B
Hetero-geneous
Homo-geneous
Distance along surface
10 r_{pr}
8 r_{pr}
6 r_{pr}
4 r_{pr}
2 r_{pr}
$D_{IZB, Flat}/D_{IZB, Spherical}$
3.0
2.5
2.0
1.5
1.0
0.001
0.010
0.100
Projectile Radius/Mars Radius

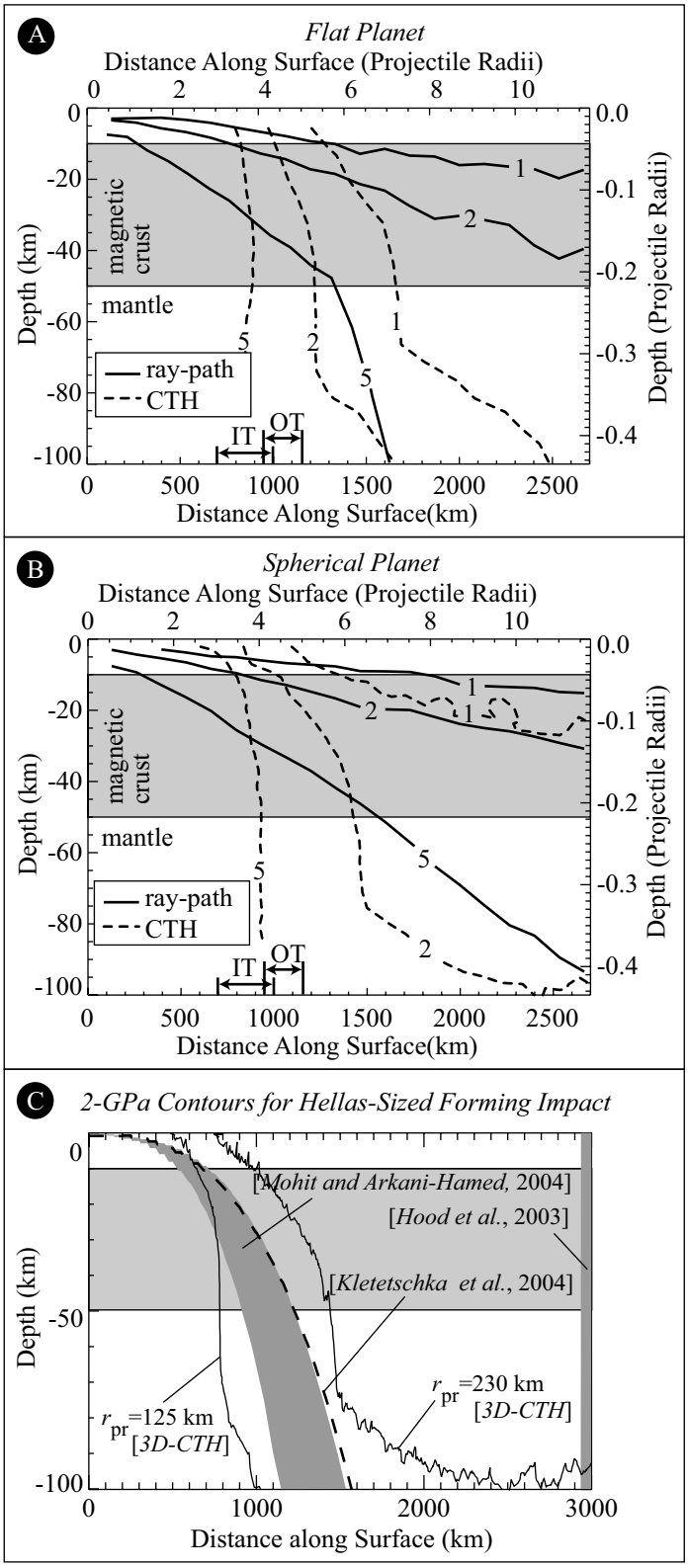
A
Flat Planet
Distance Along Surface (Projectile Radii)
0
2
4
6
8
10
0
-20
-40
-60
-80
-100
0.0
-0.1
-0.2
-0.3
-0.4
Depth (km)
Depth (Projectile Radii)
magnetic crust
mantle
ray-path
CTH
IT
OT
1
2
5
0
500
1000
1500
2000
2500
Distance Along Surface(km)
B
Spherical Planet
Distance Along Surface (Projectile Radii)
Distance Along Surface(km)
C
2-GPa Contours for Hellas-Sized Forming Impact
[Mohit and Arkani-Hamed, 2004]
[Hood et al., 2003]
[Kletetschka et al., 2004]
r pr =230 km
[3D-CTH]
r pr =125 km
[3D-CTH]
-50
-100
1000
2000
3000
Distance along Surface (km)

AUXILIARY MATERIAL
Effects of Planet Curvature and Crust on the Shock Pressure Field around Impact Basins

Karin L. Louzada, Sarah T. Stewart

Department of Earth and Planetary Sciences, Harvard University, Cambridge, MA, USA.

The auxiliary material for this article contains:

1. Figure S1: Calculations of ray path lengths for direct and reflected waves in a flat and spherical geometry.
2. Figure S2: The internal structure models for Mars.
3. Figure S3: Timestep, angle spacing and grid size sensisivity tests for the ray path model (including Table S1).
4. Description of the CTH calculations (including Table S2).
5. Table S3: Input variables for Figure 3 in the main text.
6. Figure S4: Crust-mantle boundary effects.
7. Figure S5: Evolution of the burial depth in CTH simulations.
8. Table S4: Average shock pressures in the magnetic crust of Mars for a Hellas-type event.

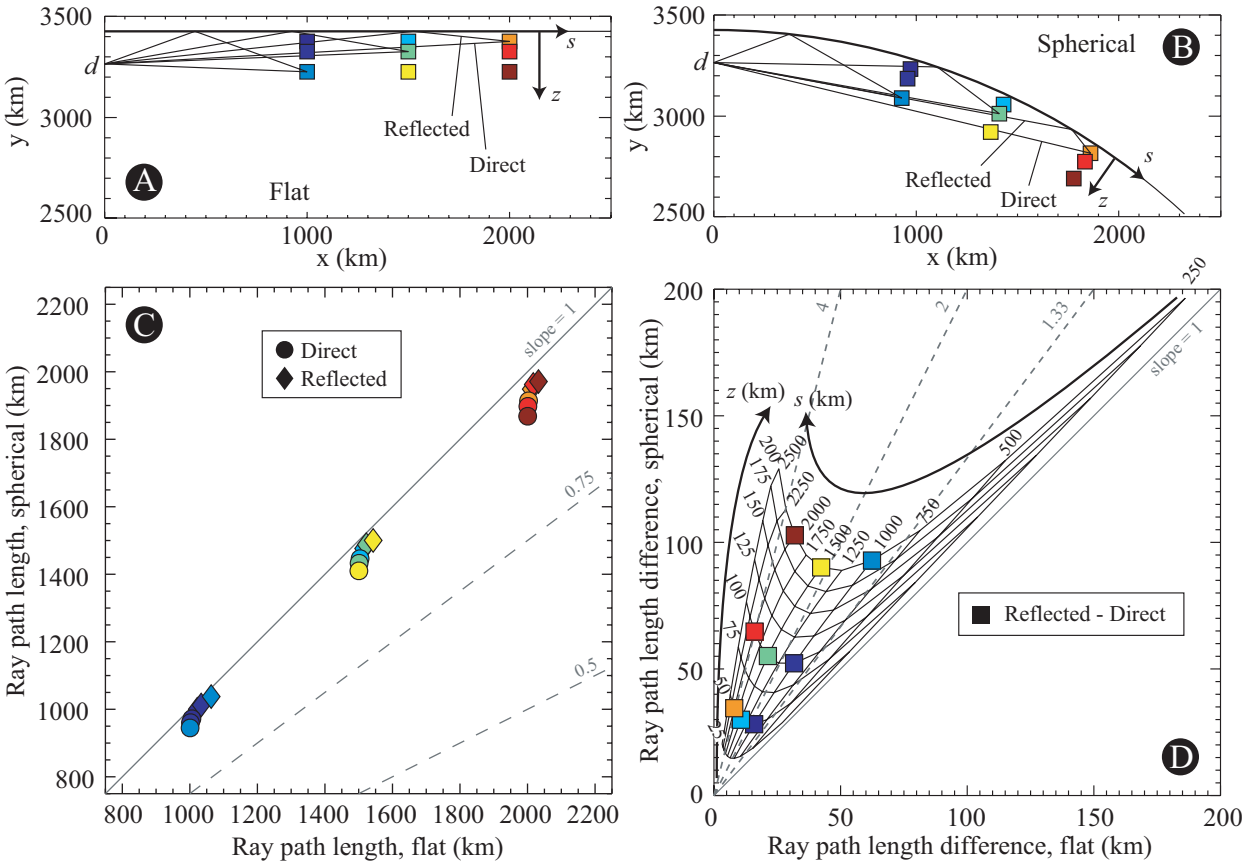

Figure S1. Direct and reflected ray paths to selected locations in at distances along the surface, *s*, (1000, 1500, and 2500 km) and depths, *z*, (50, 100, 200 km) in a (A) flat and (B) spherical homogeneous (case I) Mars . The radius of Mars is 3426 km and the burial depth is 0.7·230 km. Three example direct and reflected ray paths are drawn in both panels to show the difference in the shape of the ray paths. (C) The calculated lengths of the direct (circles) and reflected (diamonds) ray paths in the flat versus the spherical case for each are shown. As expected, the direct and reflected ray paths are shorter in the spherical planet case. (D) The difference between the reflected and direct ray path lengths for flat versus spherical planet geometries. The ray path length difference is proportional to the arrival time difference of the waves. Ray path length differences are shorter in the flat planet case, increasing with distance *s* along the surface and decreasing with depth *z*. At 1000 km from the impact, at 50 km depth (the lower limit of the crustal thickness) the ray path length difference (and the arrival time difference) is 2 times greater in the spherical planet case than it is in the flat planet case (darkest blue square).

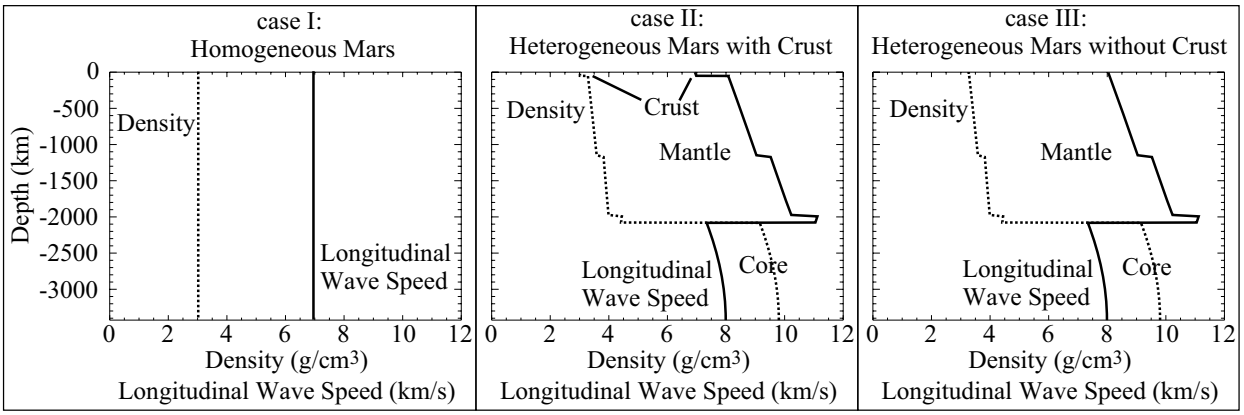

Figure S2. Internal structure models for Mars used in the ray-path and CTH calculations showing the change in density (dashed, courtesy of D. Valencia using the techniques described in [*Valencia, et al.*, 2006]) and longitudinal wave speed (black, scaled to the Preliminary Reference Earth Model, [*Dziewonski and Anderson*, 1981]). Three possible internal structures were considered: (I) homogeneous planet with a constant crustal density and sound speed. (II) a full heterogeneous Mars with a 50-km thick crust (3 g/cm^3) overlying a 2000-km thick mantle and core of 1376-km radius [*Zuber*, 2001], and (III), similar to (II) but without a crust. Phase transitions in the heterogeneous Mars occur at 1173 and 2126 km depth where olivine transforms to wadsleyite and ringwoodite transforms to perovskite and magnesiowüstite, respectively. The presence of the second transition is sensitive to the mass of the core (15% of the planet in this case). The radius of Mars is 3426 km.

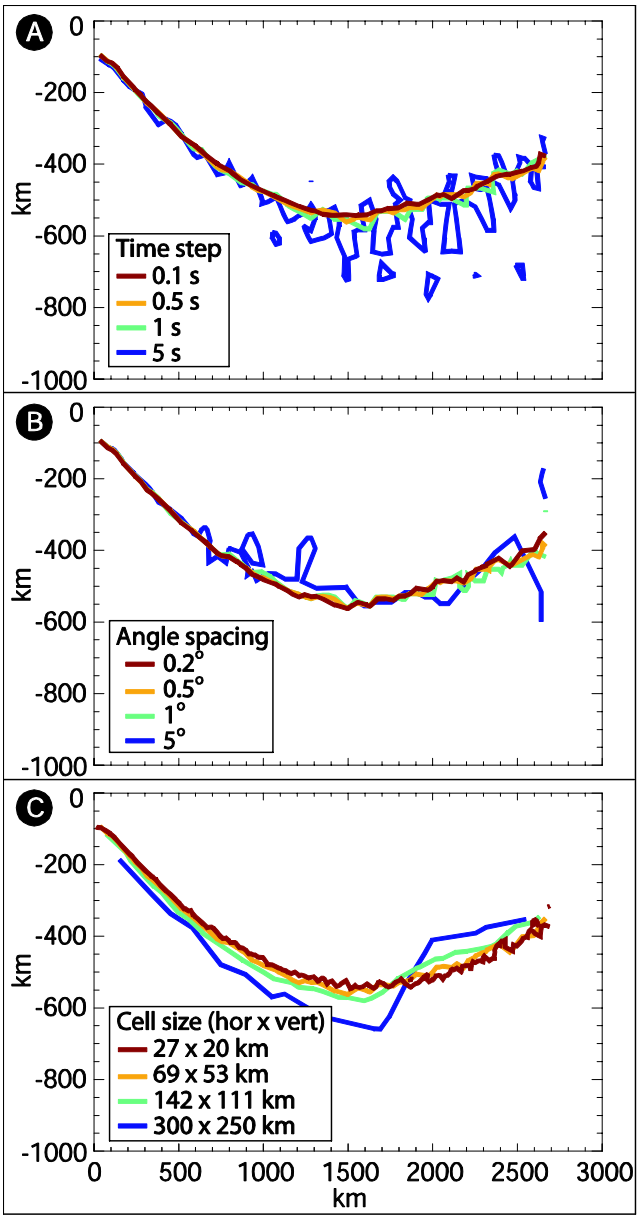

Figure S3. Tests evaluating the effects of (**A**) timestep, (**B**) angle spacing of rays emitted from the equivalent burial depth (the number of rays is indicated in Table S1), and (**C**) cell size in which the first arrivals of compressive and tensile waves are collected, on the location of the interference zone boundary. In each calculation the projectile radius is 230 km, the impact velocity is 9 km/s (vertical) and the planet geometery is spherical, using the Mars interior structure from Figure 2S. The remaining variables are indicated in Table S1. Vertical exaggeration = 2x.

Table S1. Variable input into the ray-path calculations in Figure S3, projectile radius is 230 km, the impact velocity is 9 km/s (vertical) and the planet geometery is spherical.

Panel –Color	*Timestep, seconds*	*Angle Spacing, degrees (number of rays)*	*Cell Size,km x km (hor x vert)*
A – Red	0.1	0.5 (360)	69 x 53
A – Orange	0.5	0.5 (360)	69 x 53
A – Green	1	0.5 (360)	69 x 53
A – Blue	5	0.5 (360)	69 x 53
B – Red	0.5	0.2 (900)	69 x 53
B – Orange	0.5	0.5 (360)	69 x 53
B – Green	0.5	1 (180)	69 x 53
B – Blue	0.5	5 (36)	69 x 53
C – Red	0.5	0.2 (900)	27 x 20
C – Orange	0.5	0.2 (900)	69 x 53
C – Green	0.5	0.2 (900)	142 x 111
C – Blue	0.5	0.2 (900)	300 x 250

Description of CTH calculations

CTH is an Eulerian shock physics code with multiple materials, adaptive mesh refinement, and Lagrangian tracer particles [*McGlaun, et al.*, 1990] that has been widely used in impact cratering studies. CTH version 8 has the option to include self-gravitational forces, using the parallel tree method of Barnes and Hut [1986]. We utilized tabulated equations of state [Sesame tables, see *Holian*, 1984]: projectile and crust – SiO_2 ANEOS [*Melosh*, 2007]; mantle –dunite ANEOS [*Benz, et al.*, 1989]; core – iron multiphase model [*Kerley*, 1993]. Mars was initialized with a geothermal profile (corresponding to the internal structure model in Figure S2) and three layers in gravitational equilbrium with radii of 1345, 3372, 3426 km for the core, mantle and crust, respectively. In some cases, the crust was omitted. All materials were hydrodynamic for a straightforward comparison to the wave propagation model; hence the final basin diameters were not calculated

The projectile was initialized in self-gravitational equilibrium for 3D runs and at zero pressure for 2D runs at a constant temperature of 200 K. Impacts were normal to the surface at 9 km/s. Lagrangian tracer particles were placed in the impact plane (2D tracer distribution in all cases) with greater spatial resolution near the impact point and in the crust (an example tracer distribution is shown in Figure 2).

The spatial resolution of the Eulerian grid was highest near the impact point and in the impact plane, and decreases with distance. Note that the adaptive mesh refinement scheme in CTH keeps materials adjacent to highly resolved regions at the same resolution or decreased by a factor of 2 [*Crawford*, 1999].

Table S2. Overview of CTH calculations.

Simulation Geometry	*Projectile Radius* (km)	*Mars Layers*	*Projectile Resolution* (km)	*Crust Resolution* (km)	*Mantle Resolution* (km)	*Figures*
2D	230	Mantle, core	5	----	1.25	S4C, S5B
2D	230	Crust, mantle, core	2.5	1.25	2.5	2, 4A, S4C, S5B
3D*	230	Crust, mantle, core	7.3	3.6	14.6	2, 4B, 4C, S4A, S5B
2D	125	Crust, mantle, core	2.5	1.25	2.5	
3D	125	Crust, mantle, core	3.6	3.6	14.6	4C
2D	50	Crust, mantle, core	1.3	0.63	1.25	S5B

*A 230-km radius projectile 3D case at about two times lower resolution in the projectile and crust yielded nearly identical results.

Table S3. Variables input into the ray-path calculations in Figure 3 (main text).

Projectile Radius, km	*Projectile/Mars Radius*	*Time Step, seconds*	*Angle Spacing, degrees (number of rays)*	*Cell Size, km x km (hor x vert)*
Heterogeneous Mars with Crust (red/pink)				
230	0.067	0.5	0.5 (360)	51.20 x 46.93
175	0.051	0.5	0.5 (360)	37.75 x 36.73
100	0.029	0.5	0.5 (360)	24.48 x 24.48
25	0.0072	0.1	0.1 (1800)	6.12 x 4.08
10	0.0029	0.1	0.1 (1800)	2.44 x 2.44
5	0.0014	0.1	0.1 (1800)	1.22 x 1.22
Homogeneous Mars (blue/light-blue)				
230	0.067	1	1 (180)	25.25 x 20.40
175	0.051	0.5	1 (180)	20.20 x 20.40
100	0.029	0.5	0.5 (360)	21.18 x 15.30
50	0.014	0.5	0.5 (360)	10.2 x 10.2
25	0.0072	0.1	0.5 (360)	6.12 x 6.12
10	0.0029	0.05	0.1 (1800)	2.04 x 2.04
5	0.0014	0.05	0.5 (360)	1.53 x 1.53

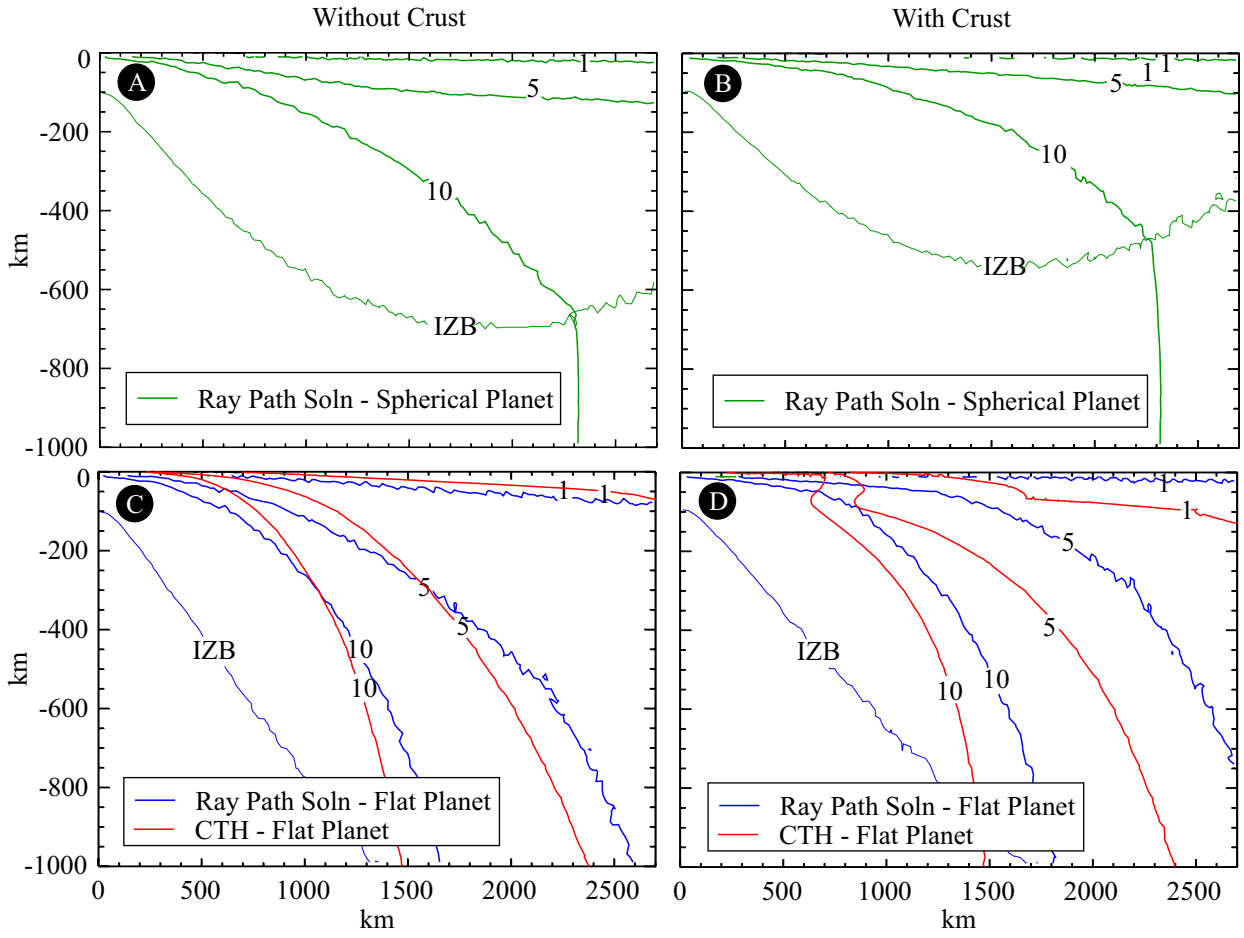

Figure S4. Tests showing the effect of including a crust in the internal structure of the planet on the peak shock pressure contours (1, 5 and 10 GPa) in (A, B) a spherical planet using the ray path solution and in (C, D) a flat planet using the ray path solution and CTH. The input variables are: projectile radius = 230 km, impact velocity = 9 km/s (vertical), time step = 0.5 s, ray spacing = 0.2 degrees, grid size = 27 x 20 km. The addition of a crust leads to shallowing of peak pressure contours near the surface in both the flat and spherical ray path calculations. The pressure contours in the ray path model for a planet without crust (B, solid) are similar to the pressure contours in the CTH calculation without crust (C, solid). The inclusion of a crust in the CTH simulation results in more complicated pressure contours (C, dashed). We infer that the ray path model does not accurately capture the effcets of the crust-mantle boundary. Vertical exaggeration = 1.7x.

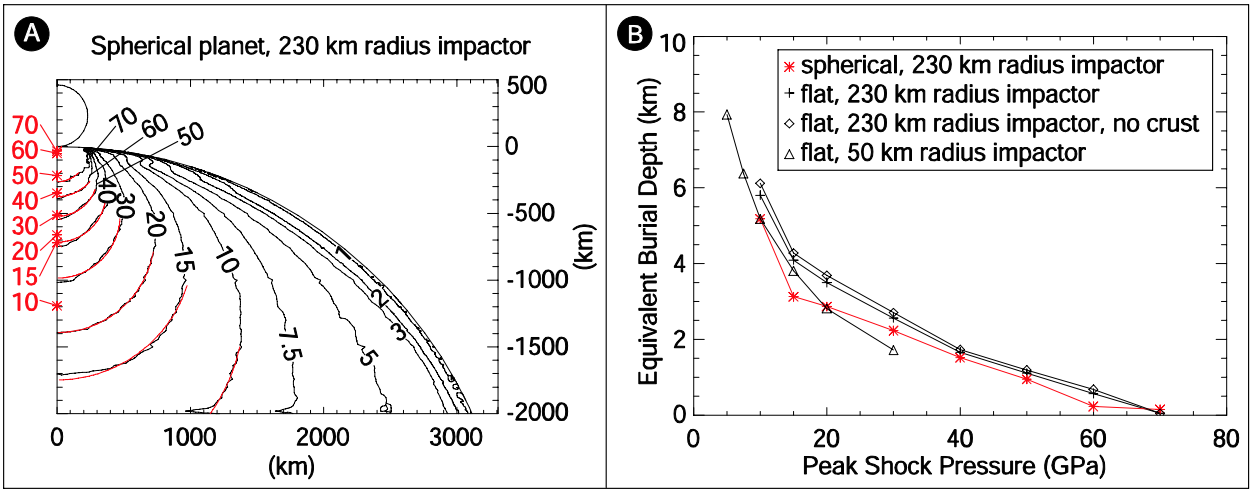

Figure S5. (A) Peak shock pressure contours (black lines) in GPa for the CTH simulation of a 230-km radius impactor onto a spherical Mars at 9 km/s. Semi-circles centered on the vertical centerline below the impact point (red lines) were fit to the pressure contours below the interference zone. The depths of the semi-circle centers are the equivalent depth of burial points for each pressure contour and are indicated by the red star symbols. No vertical exaggeration. (B) The equivalent burial depths for different pressures for four different CTH simulations are shown. With decreasing peak shock pressure the equivalent burial depth increases (see discussion of center of flow field in [*Croft*, 1980]); only for relatively high peak shock pressures (~60 GPa) is the equivalent burial depth approximately $0.7 \cdot r_{pr}$ [*Pierazzo, et al.*, 1997].

Table S4. Average shock pressure between 10 and 50 km depth on Mars from 3D-CTH calculations for a Hellas-type event.

Distance from the impact point along the surface (km)	r_{pr} = 230 (km)	r_{pr} = 125 (km)
250	54 (±17)	20 (±4.2)
500	17 (±1.5)	8.1 (±1.1)
750	8.6 (±1.1)	2.0 (±0.3)
1000	3.4 (±0.7)	1.1 (±0.2)
1250	2.1 (±0.4)	0.7 (±0.1)
1500	1.5 (±0.3)	0.6 (±0.1)

With standard deviations in parentheses. $\tau = r_{pr}/v_i$, v_i = 9 km/s, $d = 0.7 \cdot r_{pr}$.

References

Barnes, J., and P. Hut (1986), A hierarchical O(N log N) force-calculation algorithm, *Nature*, *324*, 446-449, doi:10.1038/324446a0.

Benz, W., A. G. W. Cameron, and H. J. Melosh (1989), The origin of the Moon and the single impact hypothesis III, *Icarus*, *81*, 113-131, doi:10.1016/0019-1035(89)90129-2.

Crawford, D. A. (1999), Adaptive mesh refinement in CTH Report SAND99-1118C, 10 pp, Sandia National Laboratory, Albuquerque NM.

Croft, S. K. (1980), Cratering flow fields: Implications for the excavation and transient expansion stages of crater formation, *Proc. Lunar Plan. Sci. Conf. 11th*, 2347-2378.

Dziewonski, A. M., and D. L. Anderson (1981), Preliminary reference Earth model, *PEPI*, *25* (4), 297-356, doi:10.1016/0031-9201(81)90046-7.

Holian, K. S. (1984), T-4 Handbook of Material Properties Data Bases, Vol. 1c: Equations of State Report LA-10160-MS, 382 pp, Los Alamos National Laboratory, Los Alamos, NM.

Kerley, G. I. (1993), Multiphase Equation of State for Iron, Sandia National Laboratories, Albuquerque, NM.

McGlaun, J. M., S. L. Thompson, and M. G. Elrick (1990), CTH: A 3-dimensional shock-wave physics code, *Int. J. Impact Eng.*, *10*, 351-360, doi:10.1016/0734-743X(90)90071-3.

Melosh, H. J. (2007), A Hydrocode Equation of State for SiO_2, *MAPS*, *42* (12), 2079-2098.

Pierazzo, E., A. M. Vickery, and H. J. Melosh (1997), A Reevaluation of Impact Melt Production, *Icarus*, *127*, 408-423, doi:10.1006/icar.1997.5713.

Valencia, D., R. J. O'Connell, and D. Sasselov (2006), Internal structure of massive terrestrial planets, *Icarus*, *181* (2), 545-554, doi:10.1016/j.icarus.2005.11.021.

Zuber, M. T. (2001), The crust and mantle of Mars, *Nature*, *412*, 220-227, doi:10.1038/35084163.